ACS APPLIED MATERIALS & INTERFACES

www.acsami.org

Research Article

Multifunctional Cyclized Polyacrylonitrile (cPAN) as a Coating for Sb-Based Anodes in Sodium-Ion Batteries

Daniel S. Windsor, Monika J. Perez, Erin R. Snyder, Nathan A. Neisius, Rhys A. Otten, Sarah C. Hall, Clara A. Tibbetts, Amber T. Krummel, and Amy L. Prieto*

Cite This: *ACS Appl. Mater. Interfaces* 2025, 17, 2117−2129

Read Online

ACCESS | Metrics & More | Article Recommendations | Supporting Information

ABSTRACT: Conversion electrodes, such as antimony (Sb), are high energy density electrode materials for sodium-ion batteries (NIBs). These materials are limited in their performance due to the mechanical instability of these systems resulting from volume expansion of the material during cycling. Stabilizing conversion materials using a conductive polymer binder (CPB) protective layer is an effective way to enhance the performance of these materials. There is, however, a lack of a clear understanding of how CPBs affect the (de)insertion and surface chemistry of these systems. Herein, we report the systematic investigation of the effects on Na-ion (de)insertion chemistry of a cyclized-polyacrylonitrile (cPAN) layer on Sb-based conversion electrodes in NIBS. Through electrochemical characterization, it was determined that the inclusion of a cPAN layer increases the achievable capacity of the electrode system due to the storage of Na ions by the cPAN layer and facilitates Na-ion transport to the Sb active material at early cycles by reducing the charge transfer resistance of the ensemble electrode.

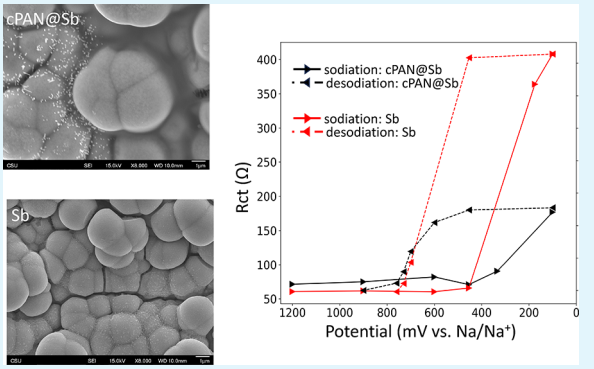

KEYWORDS: *sodium-ion batteries, cyclized-polyacrylonitrile, antimony, conversion electrodes, electrochemical impedance spectroscopy*

1. INTRODUCTION

The development of renewable energy storage technologies have garnered much attention and capital because of their potential to reduce humanity's dependence on hydrocarbon-based energy sources to mitigate the effects of climate change.[1,2] Of the many renewable energy technologies under development, secondary battery (rechargeable) technologies have become ubiquitous.[3,4] Developed in the late 20th century, lithium-ion batteries (LIBs) have become an integral part of modern life, owing to their inclusion in technologies ranging from mobile electronics to electric vehicles.[2,4,5] Despite the popularity and omnipresence of LIBs, there is no single battery technology that is perfect for every application, and as a result, LIBs are not suitable for every energy storage application due to low natural abundance of lithium, cost, and geographical availability of the materials needed for this technology.[6,7] Sodium-ion batteries (NIBs) are an exciting alternative to LIBs for large-scale energy storage applications, owing to the relative abundance of NIB feedstock materials and a lower price point ($6500/ton for Li_2CO_3, $200/ton for Na_2CO_3).[8,9] Although NIBs are an exciting alternative to LIBs for grid-level energy storage, the materials that function in the NIB system are not as well developed as are the materials for LIBs.

The NIB system is amenable to a variety of electrode materials. One class of high energy density materials for NIB anodes is conversion electrodes. Conversion electrodes differ from intercalation electrodes, such as hard carbon, in that the active ions are not stored in interstitial positions within the lattice but are incorporated into new crystallographic phases.[10−15] Of the conversion electrodes studied for application in NIBs, antimony (Sb) is one of the most popular, with a theoretical capacity of 660 mAh/g as well as good thermal stability and electrical conductivity.[16,17]

Although conversion electrode materials (such as Sb) generally have higher theoretical capacities than intercalation electrodes, these materials are all inhibited by large volumetric expansions of the material when converted to the fully sodiated phase. The (de)sodiation of Sb begins with pristine Sb, either amorphous or trigonal Sb ($R\bar{3}m$), and fully sodiates to the hexagonal Na_3Sb ($P6_3/mmc$) before returning the original Sb (amorphous or phase trigonal) during desodiation.[18] These changes in the composition of the material lead to changes of

Received: August 26, 2024
Revised: December 11, 2024
Accepted: December 11, 2024
Published: December 30, 2024

https://doi.org/10.1021/acsami.4c13887
ACS Appl. Mater. Interfaces 2025, 17, 2117−2129

up to 293% in the unit cell volume, which detrimentally affects the ability of this material to cycle stably in a battery.[17]

These volumetric changes between phases, during insertion/deinsertion of ions, are manifested in mechanical stresses and strains in the electrode material. As a result, the electrode material is pulverized, leading to a loss of reversible capacity through excessive solid electrolyte interphase (SEI) growth, and can even lead to delamination of the electrode active material from the current collector.[14,16] Thus, to include conversion electrode materials in NIBs for high energy density systems, the stabilization of these materials is imperative.

To stabilize conversion electrodes, investigators have evaluated creative approaches toward stabilizing these systems. Some of these approaches include nanostructuring the active material,[12,17,19] utilization of carbon to form composite electrodes,[20] or incorporating inactive yet mechanically robust constituents in the electrode,[14,15] as well as electrolyte optimization.[21,22] Of the many different approaches applied toward the stabilization of conversion electrodes, an increasingly popular approach is through the inclusion of conductive polymer binders (CPBs) in the electrode framework. The popularity of CPBs arises from the mechanical compliance of the polymeric layers, which alleviates the detrimental effects of the volume expansion.[12,23,24] The conductive nature of these polymers allows for pulverized pieces of active material to remain in electrical contact with the remainder of the bulk electrode.[12,25] A highly studied CPB in the LIB literature is cyclized polyacrylonitrile (cPAN), which is formed by pyrolyzing the polyacrylonitrile (PAN) precursor.[26,27] The cPAN polymer as a protective coating has been shown to enhance the performance of conversion electrodes (Si, Sn, and Sb) in a variety of electrode configurations, which is attributed to the mechanical robustness and electrical conductivity of the polymer.[11,12,28] The cPAN polymer has, also, been shown to actively store alkali metal ions as a standalone organic cathode.[28,29] In a recent study, Zhang et al. reported that a slurry cast cPAN electrode had an achievable cycling capacity of 280 mAh/g, which is comparable to the achievable capacity of hard carbon anodes in NIBs.[28]

Despite the depth of work on cPAN in the battery literature, there is a distinct lack of understanding as to how the inclusion of cPAN, as a protective coating, affects the Na-ion insertion/deinsertion and surface chemistry of the anode to which it is applied. Given the complexity of battery systems, a clear understanding of the functionality of the constituents in a battery is imperative if we are to understand how different materials impact cell degradation, leading to informed design principles. Therefore, the objective of this investigation is to study the effects of cPAN on the fundamental electrochemistry of the anode system to which it is applied. To achieve this, a layered coating-active material configuration, with the cPAN precursor (PAN) spin-coated onto thin-film electrodeposited Sb, was used. The advantage of this configuration is that it negates the convoluting effects of constituents in slurry cast electrodes on the electrochemical data and the effects of nanoscale active materials or nanofabricated structures.[16,30] For these reasons, the layered coating-active material configuration aids in the study of the fundamental interactions occurring at the electrode in question.

Herein, we report a detailed investigation aimed at characterizing the effect of a cPAN-protective layer on the fundamental (de)sodiation chemistry and surface chemistry (SEI formation) of Sb-based anodes in NIBs. We tested the effect of cPAN on the achievable capacity, initial capacity loss (ICL), Coulombic efficiency (CE), and rate capability of Sb-based electrodes through galvanostatic cycling experiments. Differential capacity (dQ/dV) analysis was used to assess the effect of cPAN on the (de)sodiation chemistry of Sb, while constant-current constant-voltage (CCCV) with electrochemical impedance spectroscopy (EIS) was used to assess the effect of cPAN on the resistive properties of Sb during cycling. A cPAN-protective coating not only increases the achievable capacity of the anode but also facilitates Na-ion conduction at the electrode−electrolyte interface.

2. EXPERIMENTAL SECTION

2.1. Electrodeposition Solution Preparation. A nickel-deposition solution was formed by adding 1.066 M $NiSO_4{\cdot}6H_2O$ (140 g, Millipore Sigma, ≥98%), 45 g/L $NiCl_2{\cdot}6H_2O$ (22.5 g, Alfa Aesar, 99.%), 0.189 M citric acid (8.5 g, Millipore Sigma, ≥99.5%), 0.0109 M sodium saccharin (1.0 g, Fisher), and 0.0023 M 2-butyne-1,4-diol (0.1 g, Millipore Sigma, 99%) to 500 mL of Millipore water (18Ω). This solution was then stirred for 30 min before being titrated to pH 4.5. An antimony deposition was formed by mixing 30 mM (1-hexadecyl)trimethylammonium bromide (CTAB, 2.18 g, Alfa Aesar, 98%) and sodium gluconate (8.64 g, Milipore Sigma, ≥99%) to 200 mL of Millipore water before being left to stir. After stirring for 5−10 min, 30 mM antimony chloride (1.37 g, Milipore Sigma, ≥99%) was added to the solution. The solution was left to stir on a stir plate overnight.

2.2. Electrodeposition of Sb@Ni@tCu. A textured copper (tCu) foil substrate was utilized in this investigation and was prepared for deposition via a washing treatment of concentrated phosphoric acid, and then water, and finally absolute ethanol for 30 s each. The nickel deposition solution was heated to 60 °C using a VWR water heater/cooler. The nickel solution was then placed in a custom deposition cell (described in the work of Nieto et al.[16]) using the cleaned tCu as the working electrode (Oak-Mitsui, TBL-DS Cu foil), a stainless-steel mesh counter electrode (316 stainless steel, Elmhurst, P.O.# AC-75973470), and a saturated calomel (SCE) reference electrode. The deposition of nickel onto the tCu working electrode occurred at −1.0 V vs SCE for 60 s, forming Ni@tCu. The remaining nickel solution was removed from the deposition cell, and the substrate was immediately rinsed thoroughly with Millipore water before the addition of the antimony deposition solution, which was then let to rest for 10 min in order to allow maximum wetting of all surfaces. The antimony deposition onto the Ni@tCu was conducted at −1.05 V vs SCE under chronocoulmbic conditions until a charge limit of 3 C/cm^2 was reached, forming Sb@Ni@tCu. The electrodeposited Sb@Ni@tCu was then washed with water and ethanol prior to storage in a vacuum desiccator. The mass of the deposited Sb was calculated from the electrochemical data using eq 1, where MW is the molecular weight of the deposited material, n is the number of electrons transferred in the reaction, F is Faraday's constant, and Q is the charged passed during the deposition.

$$m_{dep} = \frac{MW}{nF}Q \tag{1}$$

2.3. PAN Solution Synthesis. 1 M PAN in *N*,*N*-dimethylformamide (DMF) solution, based on moles on monomer units, was prepared by adding PAN powder (10.6 g, Sigma, 181315, average M/W 150,000) to DMF (200 mL, Fisher Scientific). The solution was stirred at approximately 80 °C until dissolution was established, about 3 h. The solution was allowed to cool before being used in the spin-coater setup. For the sodium bromide PAN solution, 0.5 M sodium bromide (0.5145 g, Millipore Sigma, ≥99%) was added to 1 M PAN in DMF solution, as described above.

2.4. PAN Coating Parameters. 1/2″-diameter substrates were coated with the 1 M PAN solution with an MTI VTC-100 vacuum spin coater (MTI, CR2025 spacer, SS304, Φ 15.5 mm by T 0.2 mm). Spin-coating parameters were 2000 rpm for 30 s, followed by 8000

https://doi.org/10.1021/acsami.4c13887
ACS Appl. Mater. Interfaces 2025, 17, 2117−2129

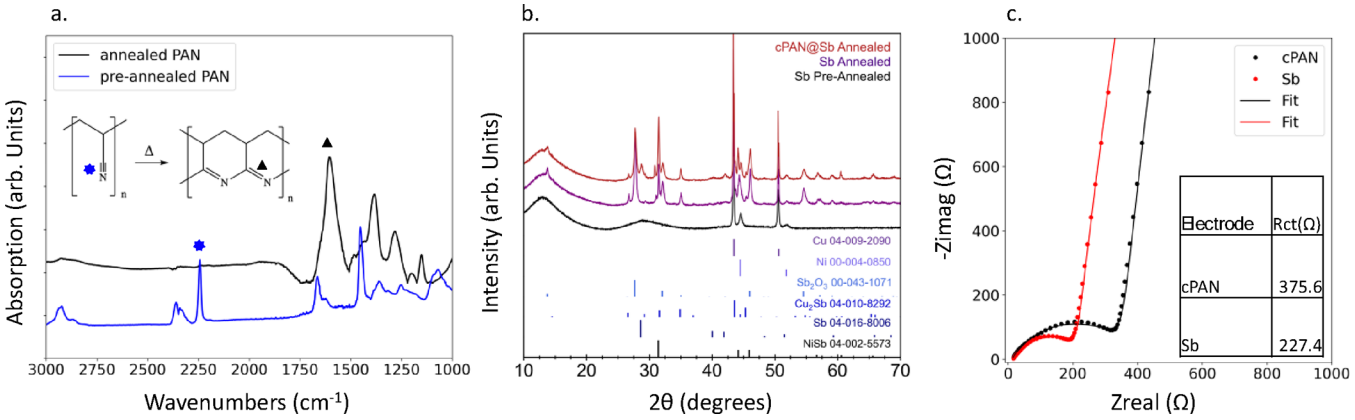

Figure 1. Material characterization of cPAN@Sb-based and Sb-based electrodes. (a) Fourier transform infrared spectroscopy (FTIR) of spin-coated polyacrylonitrile (PAN, blue) and annealed cyclized polyacrylontrile (cPAN, black). (b) Powder X-ray diffraction (PXRD) patterns of a Sb electrode, pre- and postannealing, with a cPAN@Sb-annealed pattern. (c) is an electrochemical impedance spectroscopy (EIS) Nyquist plot with cPAN@Sb-based (black) and Sb-based (red) in Swagelok half cells prior to battery cycling.

rpm for 10 s. The PAN solutions were applied to the spinning substrates with a syringe pump (Kent Scientific Corp., GenieTouch Syringe Pump). The PAN solutions were applied to the substrate at a rate of 0.5 mL/min for the entirety of the 2000 rpm step. For the 8000 rpm step, the syringe pump was stopped so that excess PAN did not build up on the substrate.

2.5. Substrate Annealing Parameters. All electrodes were annealed in a Lindberg tube furnace (model 55322-3, 2″ OD alumina tube) under flowing argon. The electrodes were placed in an alumina boat, which was positioned in the center of the tube. The tube was sealed and subsequently purged three times before argon was flowed over the sample at 60−80 mL/min. Samples were allowed to sit at ambient temperature for 30 min after the purge cycles. The temperature of the furnace was ramped to the desired annealing temperature at a rate of 50 °C/min, after which the annealing time was started. After the specified annealing time had elapsed, the samples were allowed to cool to 100 °C before the tube furnace was opened.

2.6. Battery Assembly and Cycling Conditions. Coated and uncoated substrates were assembled into Na-ion half-cells in an argon-filled glovebox (O_2 ppm <1 ppm, H_2O ppm <0.5 ppm). For the Na-ion half cells, 1 M sodium perchlorate ($NaClO_4$) was added into propylene carbonate (PC) with 5% by volume of fluoroethylene carbonate (FEC). 2032-coin cells (MTI) were utilized for cycle life and rate capability testing and were fabricated with a Na-foil counter/reference, a glass filter-paper separator (21 mm ⌀, GE Whatman), and the substrate in question with 80 μL of electrolyte before being sealed with a coin-cell press at 0.9 tons (MTI, MSK-160E). For the XPS and EIS experiments, Swagelok half cells were used where a Na-metal counter/reference, 200 μL of electrolytes, a glass filter-paper separator (21 mm ⌀, GE Whatman), and polypropylene separators (MTI, Li-ion battery separator film, 25 μm thick, batch no. 0120313) were used.

2.7. Electrochemical Testing. All electrochemical cells were allowed to rest for at least 12 h before any testing. The galvanostatic cycle life, rate capability, and formation experiments were conducted on an Arbin battery cycler (Model LBT20084 or Model BT-2143). Potentiostatic EIS experiments were conducted by using a Gamry Reference 3000 potentiostat. EIS experiments were run between 100 kHz−100 mHz with an excitation of 10 mV (RMS) vs OCV. For the CCCV, the chronopotentiometry step was conducted at ±0.00001 A, while the chronoamperometry step was held for 6 h at the desired potential selected from differential capacity (dQ/dV) analysis. Cyclic voltammetry for surface area characterization was conducted over a potential window from 2.0 to 2.6 V vs Na/Na^+. The scan rates for this experiment were 50, 100, 150, 200, and 250 mV/s. The peak current as a function of scan rate was selected at 2.3 V vs Na/Na^+.

2.8. Materials Characterization. PAN-coated samples were analyzed via FTIR spectroscopy (Bruker HYPERION 3000, Ge-ATR objective, 64 scans, freq resolution: 2 cm^{-1}, $N_{2(l)}$-cooled MCT detector). All electrodeposited substrates were characterized via powder X-ray diffraction (Bruker D8 DISCOVER DAVINCI, Cu Kα radiation) in the ARC-MMA laboratory in addition to the X-ray photoelectron spectrometer (PHI 5800 series MutliTechnique ECSA system, monochromatic Al Kα). The PXRD patterns were indexed with DRIFFRAC.EVA (Bruker, V5.2) using reference patterns for Cu (PDF 04-009-2090), Ni (PDF 00-004-0850), Sb_2O_3 (PDF 00-043-1071), Cu_2Sb (PDF 04-010-8292), Sb (PDF 04-016-8006), and NiSb (PDF 04-002-5573). Refinements were performed using TOPAS version 6 (Bruker AXS). A double-Voight approach to model both the size and strain was used to fit the peak profiles. The cif files were added on top of a predetermined instrument parameter with corrections to the surface roughness[31] and specimen displacement. Refinement parameters such as crystallite lattice parameters, size, strain, atomic occupancy, and isotopic displacement factor (beq) were refined individually for each structure in the following sequential order: Sb_2O_3, Cu, NiSb, Sb, Cu_2Sb, and Ni. The background terms (Chebychev polynomial) were also refined, which is displayed with a gray line in the refinements. Diffraction data was visualized using Python in the Jupyter Notebook v6.4.12. For the XPS experiments on electrodes after the first discharge and 10th cycle, batteries were disassembled in an argon-filled glovebox. The disassembled electrodes were then washed with 1 mL of dimethylcarbonate (DMC) and were then loaded into an air-free XPS holder described in the work of Schneider et al.[32] Scanning electron microscopy (JEOL JSM-6500F) images of precycling electrodes were taken in the ARC-ISS.

3. RESULTS AND DISCUSSION

3.1. Anode Characterization. The cyclization of PAN to form cPAN, while easily conducted through the partial pyrolysis of the polymer, is highly dependent on the temperature and time of the heating process.[26,27,33] To determine the extent of PAN cyclization from an annealing process, a 1 M PAN solution in DMF was spin-coated onto a stainless-steel disk, followed by annealing in a tube furnace under flowing argon for 4 h at 300 °C. The ATR-FTIR spectra of a PAN@stainless-steel disk (blue) and an annealed PAN@stainless-steel disk (black) are displayed in Figure 1a. The pre-annealed system shows a sharp peak at 2244 cm^{-1}, which is indicative of C−N triple-bond stretching from the nitrile group in the PAN structure.[26,33] This feature disappears upon annealing of the sample. In addition, the annealed sample displays a strong peak at roughly 1600 cm^{-1}, which relates to

https://doi.org/10.1021/acsami.4c13887
ACS Appl. Mater. Interfaces 2025, 17, 2117−2129

Scheme 1. Electrode Configurations for Fundamental Studies[a]

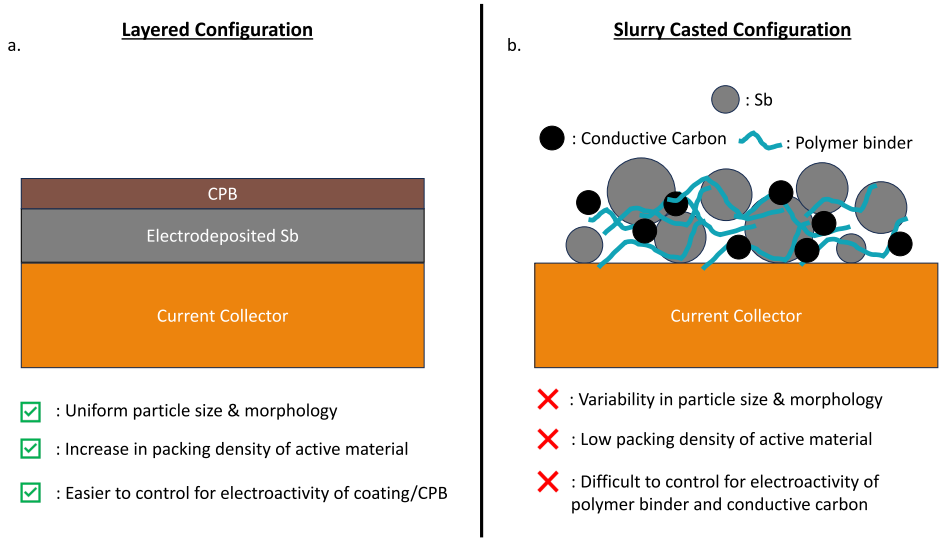

[a](a) Layered configuration of thin-film, electrodeposited, Sb on a current collector, coated by a conductive polymer binder. (b) Representation of a traditional slurry cast electrode with binders and conductive additives within the electrode system.

C−N double-bond stretching in a conjugated system.[26,34] The absence of a peak at 2244 cm^{-1} and the presence of a peak at roughly 1600 cm^{-1} indicate that the annealing process results in the cyclized PAN structure, which are in good agreement with the literature.[12,26,33,34] The broad resonances at roughly 2900 cm^{-1} in the blue spectrum relate to the extent of hydrogenation on the PAN polymer backbone.[26] The diminished intensity of this peak in the annealed PAN spectrum demonstrates that the annealing process leads to some extent to conjugation of the carbon backbone itself, which further indicates the cyclization of this material.

A thin-film, layered, active material-coating configuration (Scheme 1a) allows for fundamental insight into the effect of the cPAN coating on the electrochemistry of the Sb active material, without convoluting effects from binders and additives common in battery electrodes for NIBS (Scheme 1b). Given the temperature requirements for the cyclization of PAN, and the thin-film layered configuration for the coating/active material, it was imperative to assess how the annealing process affected the composition of the Sb thin-film deposition. After the annealing process, a conversion of the electrodeposited Sb results in the formation of crystalline Sb, Sb_2O_3, NiSb, and Cu_2Sb (Figure 1b).

The compositions of the cPAN and Sb systems were assessed via powder X-ray diffraction (PXRD) and scanning electron microscopy (SEM)/energy-dispersive X-ray spectroscopy (EDS). Preannealed films resemble previously reported diffraction data from our group, where a low-crystallinity, strained, Sb phase is represented by the broad (10-2) peak at 29° 2θ.[35] This artifact has been widely investigated and is attributed to the formation of a densely packed Sb phase (strain), while the decrease in the crystallinity is due to CTAB acting as a capping ligand for small Sb particles.[35] A Ni layer was also deposited to the tCu substrate to reduce the extent of Cu diffusion during the annealing step, which is also present in the preannealed diffraction pattern.[36] Figure S1 displays an image of an Sb@tCu electrode after the annealing step, where it is clear to see that the solid-state diffusion of the Cu into the Sb layer resulted in a mechanically unstable electrode system.[36]

The presence of surface oxides (hypothesized to be Sb_2O_3) is confirmed with SEM/EDS (Figure S2) and is further highlighted to be on the surface or amorphous due to the absence of crystalline Sb_2O_3 in the preannealed diffraction pattern. The presence of Sb_2O_3 likely arises from a surface oxide layer that becomes incorporated into the Sb electrodeposited material via the annealing process as a crystalline Sb_2O_3 phase, given that the annealing process occurs under an Ar atmosphere. The Sb−O phase diagram supports the formation of this Sb-oxide phase, which has been reported to a multicomponent Sb + Sb_2O_3 phase at temperatures close to 375 °C.[37] This temperature for Sb + Sb_2O_3 formation is higher than the annealing temperature used in this investigation; however, the presence of Sb_2O_3 under these conditions can be explained owing to the reduced pressure (between −0.05 and −0.1 MPa) utilized for the annealing of the PAN polymer.

The NiSb and Cu_2Sb phases arise from the solid-state diffusion of Ni and Cu from the substrate into the Sb material during the annealing step, which occurs due to the thin-film (layered) electrode configuration used in this study. The formation of the Cu_2Sb phase has been shown to occur to Sb thin films deposited onto Cu-current collectors when annealed at 300 °C, which is also supported by the Cu−Sb phase diagram, which shows that this phase can form at roughly 260 °C.[38,39] Assessment of the Ni−Sb phase diagram also helps to explain the presence of the Ni−Sb phase, which can form at the temperatures used in the annealing process for this investigation.[40] Quantitative analysis of the PXRD patterns in Figure 1b was conducted via Rietveld refinements, as represented in Figure S3. The refinements show that most of the crystalline phases are composed of Sb_2O_3 in both the cPAN@Sb and Sb systems, with small amounts of crystalline NiSb and Cu_2Sb. Concerning Sb, the refinements shown in Figure S3 are consistent with the results of the work of Nieto et al., which has been shown to be low-crystallinity, mostly amorphous, bulk Sb.[35] The refinements, in both systems, display peaks at roughly 30 and 60° 2θ, which were unable to be assigned with the reference PDFs used for these analyses. These phases likely relate to minor byproducts from the

https://doi.org/10.1021/acsami.4c13887
ACS Appl. Mater. Interfaces 2025, 17, 2117−2129

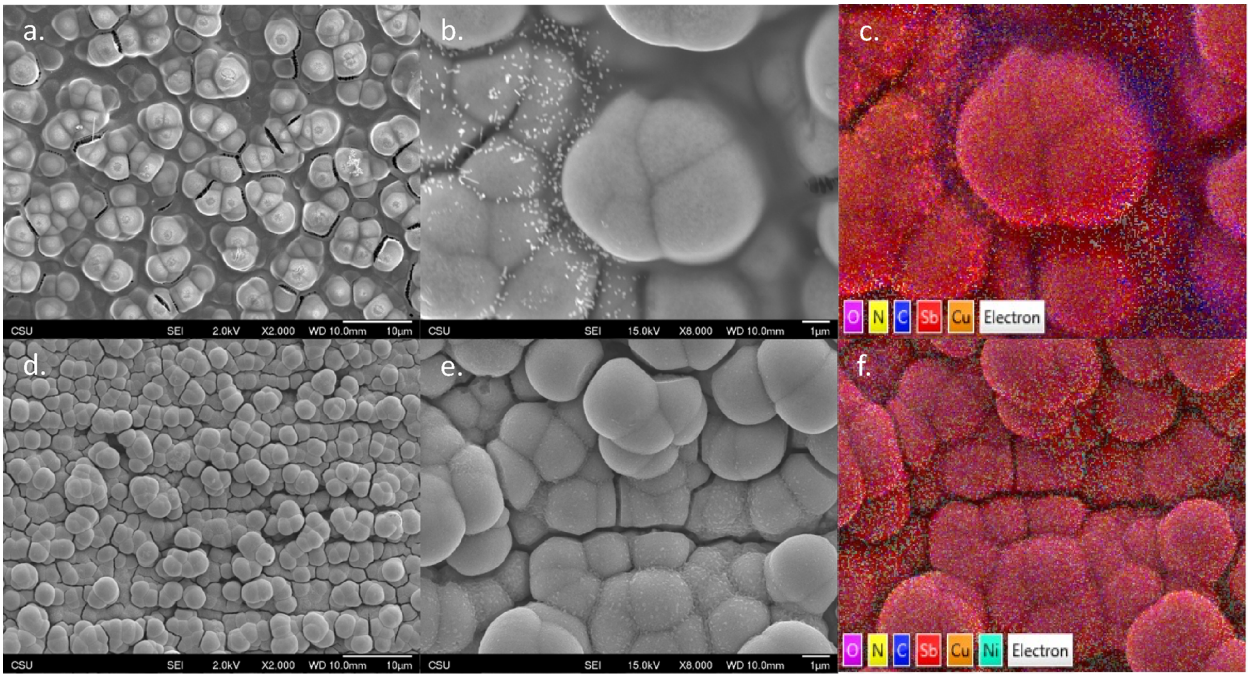

Figure 2. Scanning electron microscopy (SEM) with X-ray energy-dispersive spectroscopy (EDS) characterization of annealed cPAN@Sb and Sb systems. (a) SEM image of a precycled cPAN@Sb electrode at 2000× magnification with an accelerating voltage of 2 kV. (b) SEM image of a precycled cPAN@Sb electrode at ×8000 magnification with an acceleration of 15 kV where (c) is the accompanying EDS elemental map. (d) SEM image of a precycled Sb electrode at ×2000 magnification with an accelerating voltage of 2 kV. (e) SEM image of a precycled Sb electrode at ×8000 magnification with an accelerating of 15 kV where (f) is the accompanying EDS elemental map.

annealing process and could consist of a ternary Cu−Ni−Sb phase or an NiSb phase of a different crystal structure to the NiSb assigned in the refinements (Figure S3). Raw Rietveld Refinement data, with weight percentages and weight percent errors, are reported in the Supporting Information.

Given the mixed composition of the resulting film, the mass of the active material was determined from the charge passed during the Sb electrodeposition, as described by eq 1. In other words, the active material mass used to normalize the electrochemical data in this investigation accounts for the ensemble Sb present in the film, regardless of the extent of Ni, Cu, or O incorporation. The presence of cPAN at the annealed Sb film does not appreciably change the composition of the film, compared to the annealed Sb film without the cPAN, which serves for the purposes of studying the fundamental impact of cPAN on the (de)sodiation and surface chemistry of Sb.

The morphology and composition of the cPAN@Sb and Sb systems after the annealing process were determined via SEM/EDS, as shown in Figure 2. The electrodeposited Sb-based system retains the cauliflower-shaped structure in accordance with previous works from our group.[14,35] The inclusion of the cPAN layer does not change the structure of the Sb particles; instead, the cPAN polymer acts to fill in the gaps between the Sb domains (Figure 2a and Figure 2b). Elemental mapping with EDS for the cPAN@Sb (Figure 2c) and Sb (Figure 2f) systems demonstrates that the compositions of the post-annealed films are similar, in accordance with the PXRD results from Figure 1b. Elemental EDS maps of each identified element are displayed in Figures S4 and S5 for the cPAN@Sb and Sb systems, respectively. In the elemental map of the cPAN@Sb and Sb systems, uniform distribution of Sb, Cu, and O over the bulbous Sb features is observed. In Figure S3, the carbon distribution is concentrated at the spaces between the Sb features in the thin film, which implies that the cPAN is centered at the void spaces between Sb bulbs.

The thickness of the spin-coated and annealed cPAN was determined via cross-sectional SEM of a spin-coated cPAN@Si-wafer (Figure S6), which resulted in a cPAN thickness of roughly 250 nm. Even though cPAN inclusion to an Sb electrode resulted in an Sb film with filled-in gaps between the Sb particles, the electrochemical active surface area (ECSA) of the cPAN@Sb-based (4.79 ± 0.59 cm^2) system was larger than that of the Sb-based (3.84 ± 0.40 cm^2) system alone (Figure S7). This difference in the ECSA may result from the porosity of the cPAN layer.[29]

Indentation testing of the cPAN and Sb systems, prior to cycling, demonstrated that the inclusion of cPAN to the Sb electrode increased the hardness of the electrode system, as shown in Figure S8. As seen in Figure S8e, the Vickers hardness for the cPAN@Sb system was 42.5 Hv, while the Sb system had a Vickers hardness of 32.5 Hv. A study by Moon et al. demonstrated the correlation between particle hardness and cycling performance in lithium-ion battery cathodes; however, this notion has yet to be validated for anodes in NIBs.[41] It must be noted that these measurements relate to the entire electrode and not solely cPAN. Despite the lack of information on the mechanical properties of cPAN, these measurements do provide insight into the effect of cPAN on the hardness of the ensemble Sb-based electrode and thus the structure's resistance to local plastic deformation, which is the purpose of the investigation herein. As seen in the hardness plot, the inclusion of cPAN in the Sb-based electrode does improve the hardness of the entire electrode system, which we would expect to increase the cycle life of the Sb electrode to which the cPAN is applied.

https://doi.org/10.1021/acsami.4c13887
ACS Appl. Mater. Interfaces 2025, 17, 2117−2129

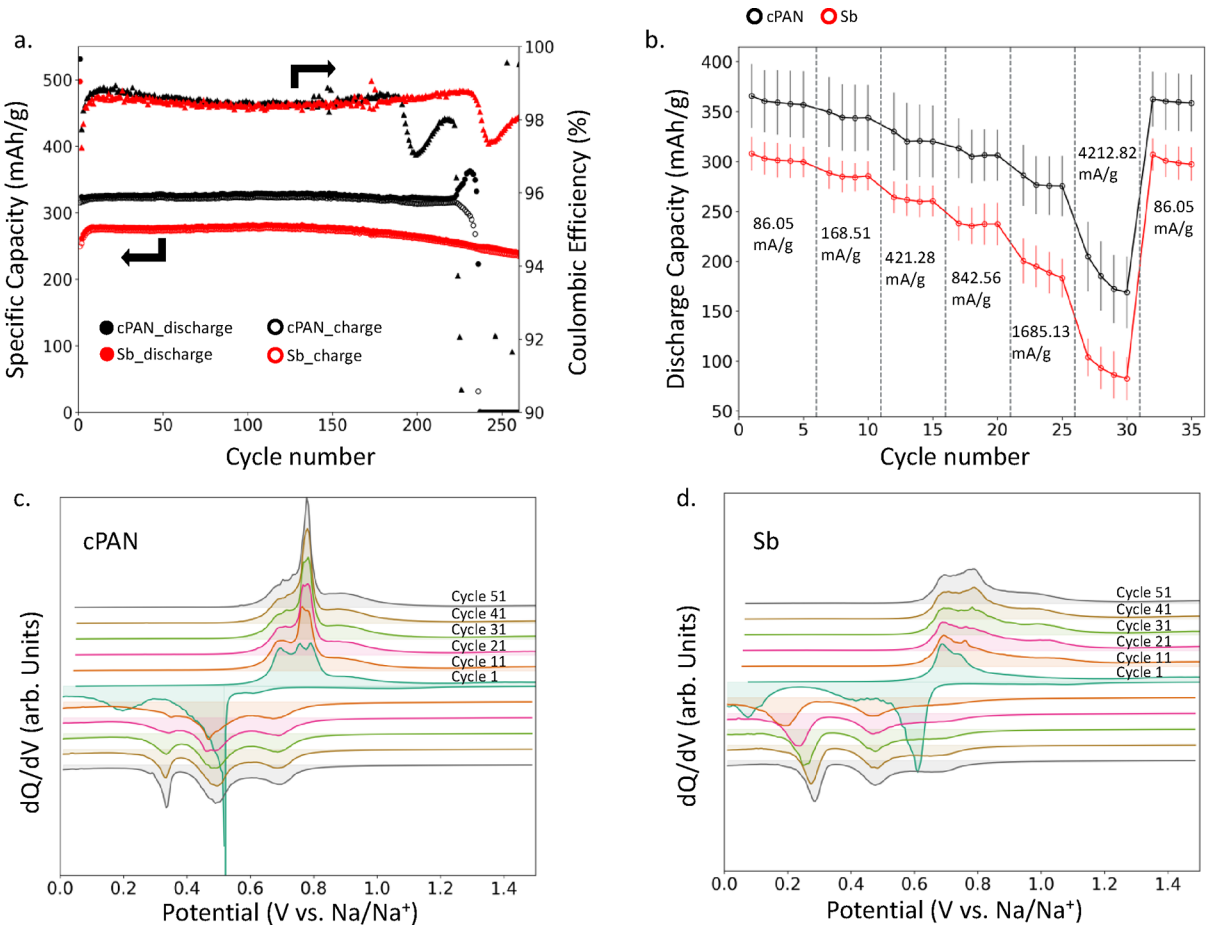

Figure 3. Electrochemical characterization of cPAN@Sb-based and Sb-based electrodes. (a) Galvanostatic cycling data and Coulombic efficiency of cPAN@Sb-based (black) and Sb-based (red) electrodes in Na-ion half cells at a rate of 117.16 mA/g. The cPAN@Sb-based system has higher capacity and lower initial capacity loss compared to the Sb-based system. (b) Rate capability testing of cPAN@Sb-based (black) and Sb-based (red) electrodes plotted with 90% confidence intervals. The cPAN@Sb-based system has better rate capability compared to the Sb-based control. (c) and (d) related to offset differential capacity (dQ/dV) plots of cPAN@Sb and Sb electrodes, respectively.

The charge transfer resistance (R_{CT}), characterized by EIS, of the pristine cPAN@Sb-based electrode was greater than that of the pristine Sb-based system alone, as shown in Figure 1c. The EIS spectra were fit to a modified Randles equivalent circuit model, which has been previously used for the analysis of Sb anodes in NIBs, as seen in Figure S9 with the fitting data being present in Table S1.[20,35,42] Although cPAN has mixed conducting properties, most of this conductivity likely arises from the conjugated polymer backbone provided by the cyclization of this material.[33] As such, we initially hypothesized that the cPAN system would have a higher charge transfer resistance (R_{ct}) compared to the Sb-based system, given that the polymer layer should impede the passage of Na ions, which is supported by the pristine EIS analysis. This implies that the cPAN system should have lower ICL than the Sb control and points to the notion that the cPAN may not be behaving solely as a conductive film.

3.2. Electrochemical Characterization. Inclusion of the cPAN in the Sb anode increases the achievable capacity and reduces the ICL compared to the bare Sb system. The most straightforward approach toward assessing the effect of cPAN on the charge storage capabilities of Sb is through galvanostatic (constant current) cycling of the two battery systems to conduct cycle life analysis. Cycle life analysis assesses how the cPAN affected the capacity, ICL, and CE of the cPAN and Sb systems (Figure 3a). The voltage (voltage capacity) profiles for the cPAN@Sb and Sb cycling experiments, plotted from cycles 1 to 51 in increments of 10 cycles, can be found in Figure S10. In the literature, cPAN has been shown to actively store Na ions in the work of Zhang et al.,[28] which reported a realized Na-ion storage capacity of 280 mAh/g. Second, cPAN is well known in the literature to stabilize conversion electrodes due to the mechanical properties of the polymer.[12,24] As such, we hypothesized that the cPAN layer should provide a higher capacity than the Sb-based system, which should result in distinct (de)sodiation features from the cPAN, in addition to the (de)sodiation features of Sb in an NIB system. We would also expect the cPAN@Sb-based system to have a lower initial CE and a large ICL given the increased resistance provided by the cPAN, as seen in Figure 1c. Contrary to our initial hypothesis, the ICL for the cPAN was 215 mAh/g, while for the Sb system, the ICL was 247 mAh/g. These differences in the ICL may result from the added charge storage capabilities of the cPAN polymer on the ensemble electrode. These systems also displayed CE values of 98−99%, which is consistent with the Coulombic efficiencies reported by the work of Nieto et al.[35]

To confirm that the cPAN layer was itself contributing the capacity of the anode, cPAN slurry cast electrodes were fabricated with conductive carbon and a PVDF binder, like the

https://doi.org/10.1021/acsami.4c13887
ACS Appl. Mater. Interfaces 2025, 17, 2117−2129

work of Zhang et al. These electrodes were prepared as detailed by the work of Nieto et al.[16] and were cycled in 2032-coin cells at a rate of 14 mA/g, which can nominally be described as a rate of C/20. The potential window for these cells was 0.15 to 1.5 V vs Na/Na^+ to omit any contributions to the recorded capacity from Na plating/stripping at the electrode. As seen in Figure S11, cPAN slurry cast electrodes did store Na ions stably for 50 cycles, but at a significantly lower capacity (roughly 25 mAh/g) compared to what has been reported in the literature.[28] Despite the differences in the realized capacity between this study and the work of Zhang et al., the data in Figure S11 clearly demonstrate that cPAN is capable of reversibly storing Na ions. The mechanism by which cPAN stores Na ions is certainly nonfaradic in nature, as seen in the differential capacity plots in Figure S11, indicated by the offset from zero for both the sodiation and desodiation half cycles with no sharp/distinct features in the plot. Due to the lack of distinct features in the dQ/dV plot in Figure S11d, and the small magnitude of the (de)sodiation features, it was expected to be difficult to assess exactly how the cPAN affected the (de)sodiation chemistry of the Sb anode.

An interesting feature of the cycle life analysis can be found at the point where both systems begin to display signs of failure. At roughly 225 cycles in Figure 3a, the CE of the cPAN system dramatically decreases, which is shortly followed by a sharp decrease in the charge capacity with a sharp increase in the discharge capacity. These features imply that as the cycle number increases, the cPAN system can accept charge more easily than it is able to release it. This decay feature in the cycle life plot may result from delamination of the cPAN and Sb from the current, exposing the electrode to fresh electrolyte resulting in the irreversible consumption of charge due to SEI formation.[14] The worse cycle life performance for the cPAN system in this study, contrary to the consensus in the field, likely arises from the electrode-polymer layer configuration. Traditionally, in the field, cPAN is used to stabilize conversion materials on the nanoparticle scale in a core−shell configuration, which results in the alleviation of the effects of volume expansion of the core by the shell (cPAN) in three dimensions.[12] This, then, suggests that a nanostructured or composite electrode configuration is necessary to achieve cycle life improvements with the cPAN-protective coating. While the layered coating-active material did not provide for the expected cycle life improvement usually seen with the cPAN-coated electrode, it did provide this investigation with a system capable of highlighting and deconvoluting degradation effects for these systems.

Rate capability tests demonstrated that the cPAN has a higher capacity and better capacity retention as a function of rate compared to the Sb system (Figure 3b). The use of rate capability tests provides information into how the electrode system in question functions with increasing current loads, which is preliminary information on the achievable power density of the system. These rate tests were conducted at the increasing current densities (86.05, 168.51, 421.28, 842.56, 1685.13, 4212.82, and 86.05 mA/g) over 36 cycles following a 10-cycle formation period, plotted with 90% confidence intervals. Concerning the capacity retention as a function of rate, the cPAN system retained 90.5% of the capacity upon transitioning from 842.56 to 1685.13 mA/g, and 65.6% upon the transition from 1685.13 to 4212.82 mA/g. The Sb system retained 80.9% of the capacity upon transitioning from 842.56 to 1685.13 mA/g, and 47.7% upon the transition from 1685.13 to 4212.82 mA/g. These results demonstrate that the inclusion of cPAN to an Sb-based electrode increases the overall capacity and capacity retention as a function of rate. This may arise from the mechanical stabilization from the increased hardness, which could confer an overall resistance to self-pulverization of the cPAN@Sb-based system, or a difference in the composition of the SEI at the anode-electrolyte interface provided with cPAN. While these rate capability tests provide information on electrode capacity as a function of rate, they do not provide any insight into the effect of cPAN on the (de)sodiation chemistry of Sb.

The cPAN layer most affected the early cycle (de)sodiation chemistry of the Sb anode to which it was applied. Initially, we hypothesized that the cPAN layer, given its activity toward Na ions, would affect the observed (de)sodiation chemistry of the ensemble electrode. To test this hypothesis, differential capacity (dQ/dV) plots were generated to assess where the potential landscape the major (de)sodiation events occurred for the cPAN@Sb-based and Sb-based systems. The data used to generate the dQ/dV plots can be found in Figure S10, where the differential of the raw data displayed in the voltage profiles is taken such that the plateaus in the voltage profiles turn into peaks in the dQ/dV plots. Figure 3c and Figure 3d displays the dQ/dV plots in increments of 10 cycles from the first cycle to the 51st cycle for the cPAN@Sb-based and Sb-based systems, respectively. The first cycle in both Figure 3c and Figure 3d displays a distinct electrolyte reduction peak at roughly 500 mV vs Na/Na^+ for the cPAN system, and 600 mV vs Na/Na^+ for the Sb system, which is indicative of SEI formation.[43] The increase in the overpotential for the electrolyte reduction in the cPAN system is attributed to the larger R_{ct} of the cPAN system, which is displayed in Figure 1c. Concerning cycles 11, 21, and 31 in Figure 3d, the main sodiation peak for the Sb-based system occurs at significantly more negative potentials (roughly 100 mV vs Na/Na^+), which transitions to more positive potentials as a function of cycle number. This behavior likely arises from the excess energy required to break the M−Sb or O−Sb bonds present in the starting material, as shown in Figure 1b. For the cPAN system at early cycles, the main sodiation peak arrives at significantly more positive potentials (roughly 450 mV vs Na/Na^+), which implies that the cPAN facilitates the sodiation of Sb, despite the increased interfacial resistance of the pristine electrode. These differences in the dQ/dV plots for the initial cycles of the cPAN@Sb-based and Sb-based electrodes are of great interest and point to the importance of both the interfacial chemistry and resistance phenomena over the applied potential window. By the 51st cycle, both systems display three distinct sodiation events, which are representative of the sodiation of electrodeposited Sb electrodes seen in previous works by this group.[16,35] Concerning the desodiation events, the cPAN system has many more distinct features at the main desodiation event compared to the Sb system. At roughly 1.0 V vs Na/Na^+, both systems display a broad shoulder after the main desodiation event, which is indicative of Sb_2O_3 desodiation, as seen in a previous work.[16] The results of the electrochemical experiments demonstrate that the inclusion of cPAN increases the capacity and improves the rate capabilities of the Sb anode.

The increase in the capacity results from the charge storage capabilities of the cPAN polymer, while the improved rate capability is attributed to the improved hardness of the electrode system (Figure S8) or differences in the as-formed SEI. Interestingly, despite the improved hardness provided by

https://doi.org/10.1021/acsami.4c13887
ACS Appl. Mater. Interfaces 2025, 17, 2117−2129

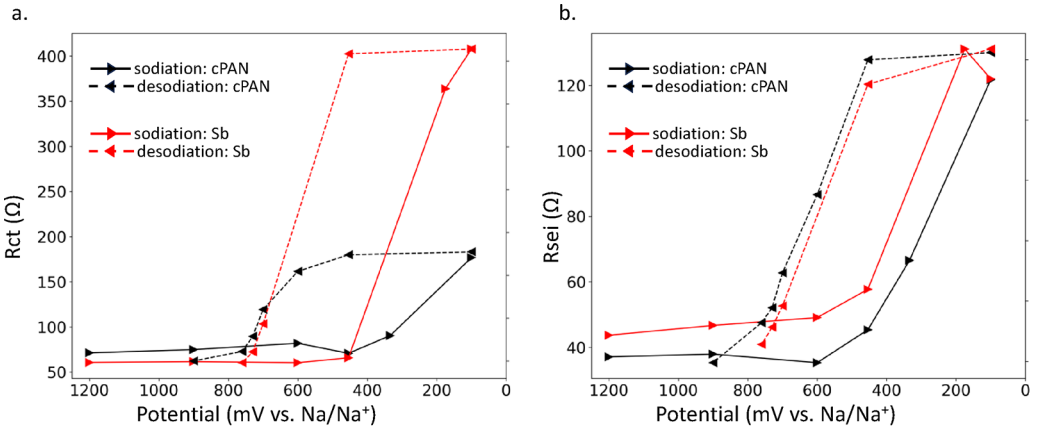

d.

Electrode system	Rct @ 0.1V vs. Na/Na^+ (Ω)	Rsei @ 0.1V vs. Na/Na^+ (Ω)
cPAN@Sb	176.8	121.7
Sb	407.9	122

Figure 4. Electrochemical impedance spectroscopy analysis of cPAN@Sb and Sb electrodes as a function of potential. (a) Charge transfer resistance (R_{ct}) plotted as a function of potential with the sodiation sweep being represented by the solid line, while the dashed line relates to the desodiation sweep. (b) Solid electrolyte interphase resistance (R_{SEI}) plotted as a function of potential with the sodiation sweep being represented by the solid line, while the dashed line relates to the desodiation sweep. (c) Schematic representation of the modified Randles circuit used to fit the EIS data. (d) Table representing the R_{ct} and R_{SEI} values for the cPAN@Sb and Sb systems at 0.1 V vs Na/Na^+ at the 10th cycle.

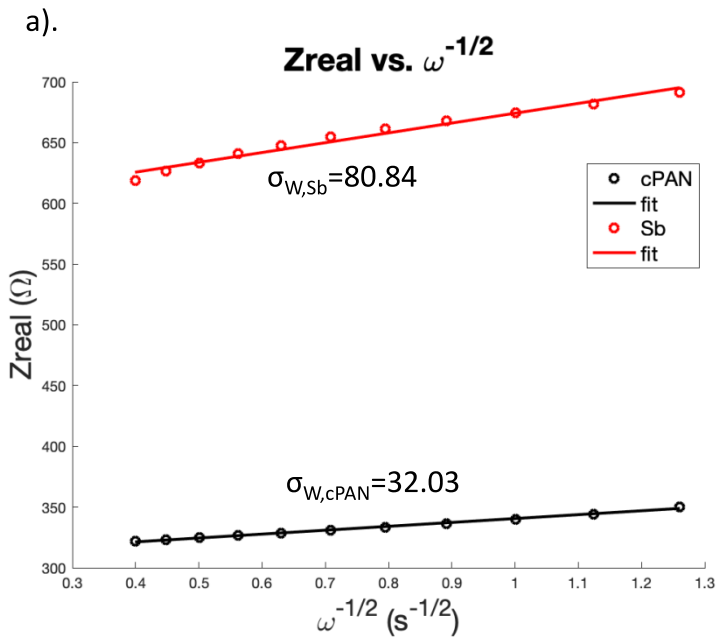

b).

$$Z_{re}=R_{sol}+R_{ct}+\sigma_w\omega^{-1/2}$$

c).

$$D_{Na}=\frac{R^2T^2}{2A^2n^4F^4C^2\sigma_w^2}$$

d).

Electrode system	D_{Na} ($cm^2\ s^{-1}$)
cPAN@Sb	2.29×10^{-16}
Sb	7.72×10^{-17}

Figure 5. Na-ion diffusion coefficient calculations. (a) Real impedance plotted as a function of the inverse of the square root of angular frequency for the low-frequency region (0.1 to 1.0 Hz), where the slope is the Warburg coefficient (σ_w). (b) Equation relating the real impedance (Z_{re}) to the Warburg coefficient. (c) Equation used for calculating the D_{Na} of the cPAN@Sb and Sb electrodes. (d) Table displaying the D_{Na} for the cPAN@Sb and Sb electrodes at the 10th cycle and at 0.1 V vs Na/Na^+.

the polymer, the cPAN system had a shorter cycle life compared with the Sb control, which likely occurs from delamination of cPAN@Sb from the current collector. This is likely an artifact of the coating-active material configuration used in this investigation (layered configuration, Scheme 1b) and suggests that nanostructuring of the coating and active material is crucial to achieving the cycle life improvements from cPAN seen in the literature. Concerning the effect of cPAN on the Sb (de)sodiation chemistry, we see that the cPAN helps to facilitate Na-ion insertion at more positive potentials than in the Sb system over the first 40 cycles or so. While these results demonstrate the effect of cPAN on the early cycle (de)sodiation chemistry of Sb, they do not provide insight into how cPAN affects the resistive nature of the Sb active material as a function of potential. Although these results clearly show that cPAN influences the cycling performance and early cycle chemistry of Sb, they do not examine how the cPAN is affecting these changes. To address how cPAN is

https://doi.org/10.1021/acsami.4c13887
ACS Appl. Mater. Interfaces 2025, 17, 2117−2129

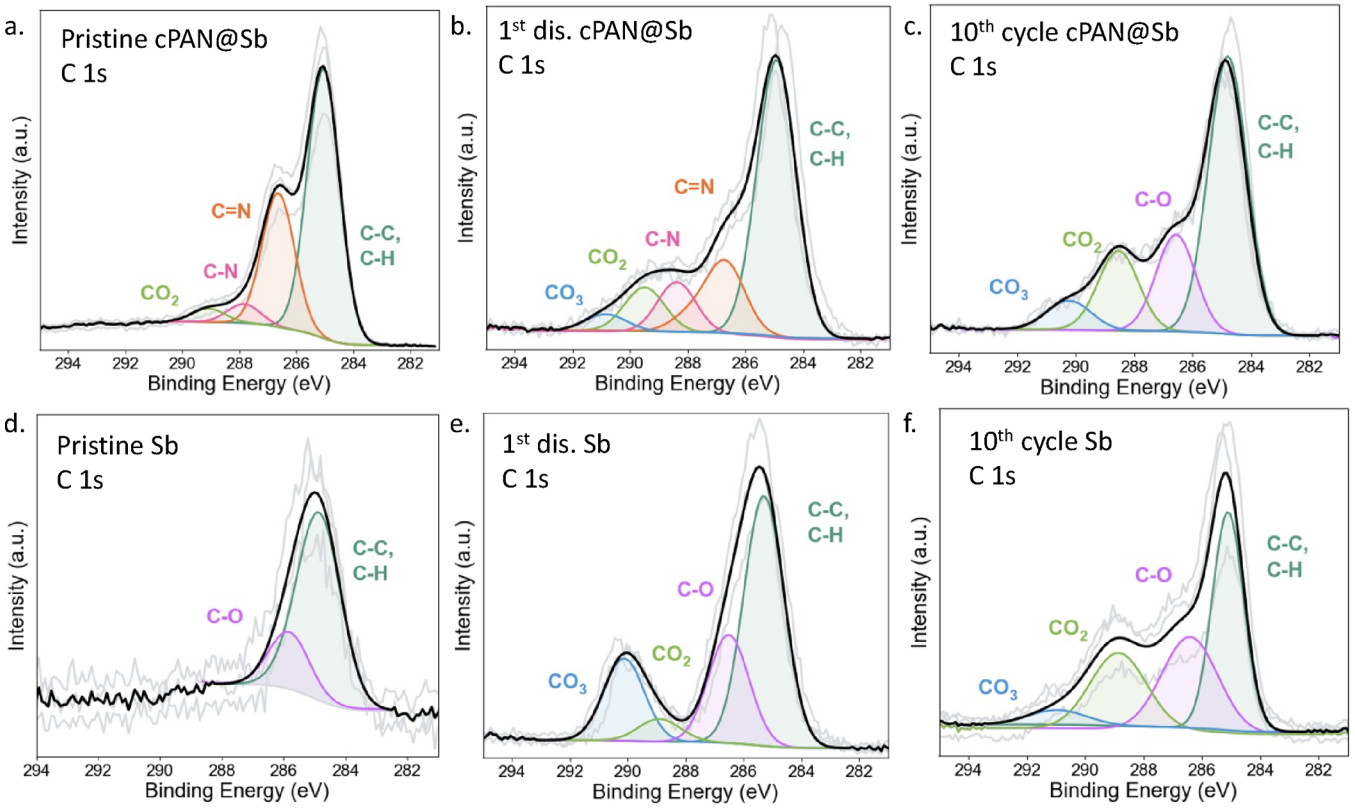

Figure 6. Electrode surface chemistry characterization was performed with X-ray photoelectron spectroscopy (XPS). (a) The C 1s spectra for the pristine cPAN@Sb electrode demonstrate CO_2, C−N, C═N, C−C, and C−H environments. (b) C 1s spectrum for a cPAN@Sb electrode after the 1st discharge half cycle, which displays CO_3, CO_2, C−N, C = N, C−C, and C−H environments. (c) The C 1s spectra for a cPAN@Sb electrode after the 10th cycle, which display CO_3, CO_2, C−O, C−C, and C−H environments. (d) The C 1s spectra for the pristine Sb electrode demonstrate C−O and C environments. (e) The C 1s spectra for an Sb electrode after the first discharge half cycle, which display CO_3, C−C, and C−H environments. (f) The C 1s spectra for an Sb electrode after the 10th cycle, which display CO_3, CO_2, C−O, C−C, and C−H environments.

affecting the Sb electrode, it is imperative to consider how cPAN affects the resistive properties of the ensemble electrode during cycling.

Analysis of the resistive properties, as a function of potential, demonstrates that while cPAN reduces the R_{ct} of the electrode system, the R_{SEI} of the cPAN and Sb systems are very similar. These parameters were determined through the application of CCCV (Figure S12a and Figure S12b) polarization for EIS analysis at the potentials where the major (de)sodiation appeared over the potential window. Figure S12c and S12d displays the dQ/dV plots of a 10-cycle formation period for the cPAN@Sb and Sb systems, respectively. The arrows indicate the potentials at which EIS spectra were taken. Figure S13 displays the EIS spectra of the sodiation sweep for the cPAN system at the indicated potentials of interest. The EIS spectra collected at the desired potentials were fit to a modified Randles equivalent circuit model with the inclusion of an SEI component, as shown in Figure 4c. The data from the application of the modified Randles circuit can be found in Tables S2 and S3 for the CCCV-EIS analyses for the cPAN@Sb and Sb systems, respectively. In the model, the $R_{SEI}||C_{SEI}$ components model the impedance behavior related to the movement of ions through the SEI. Specifically, the R_{SEI} models the resistance related to the movement of ions in the SEI, and the C_{SEI} models reactance related to the capacitive (charge accumulation) effects of the SEI. This model has been used in the literature to evaluate the impedance response of Sb electrodes in an NIB half cell.[20,35] Figure 4a and Figure 4b displays the R_{ct} and R_{SEI} plotted as a function of potential for the cPAN@Sb and Sb systems, respectively. The R_{ct} and R_{SEI} values for the EIS spectra taken at 0.1 V vs Na/Na^+ for the 10th cycle sodiation sweep are displayed in Figure 4d. In Figure 4a, it is clear to see that the cPAN has a smaller R_{ct} over the potential window compared with the Sb system. Interestingly, the R_{SEI} for both systems are very similar. These results imply that while the cPAN aids in lowering the resistance of the charge transfer process during Na-ion insertion into the Sb electrode, it does not measurably affect the impedance properties of the as-formed SEI layer. The lack of differences in the R_{SEI} for these two systems leads to the notion that the cPAN layer does affect the composition of the SEI formed while the battery is cycling, despite the potential differences of the main sodiation events at early cycles. Another important factor to consider is how the cPAN-protective layer affects the Na-ion diffusion coefficient for the ensemble electrode.

The calculated Na-ion diffusion coefficients (D_{Na}) for the cPAN@Sb and Sb systems were 2.29×10^{-16} and 7.73×10^{-17} cm^2/s, respectively (Figure 5d). This work calculated the D_{Na} at 100 mV vs Na/Na^+ after the 10th cycle to assess how the cPAN layer affected the Na-ion diffusion in the ensemble electrode. These parameters were used for the D_{Na} calculations given the clear dependence on the calculated diffusion coefficients based on the cycle number and state of charge of the electrode under examination.[44,45] Figure 5a displays the real impedance plotted as a function of the inverse of the

https://doi.org/10.1021/acsami.4c13887
ACS Appl. Mater. Interfaces 2025, 17, 2117−2129

square root of the angular frequency over the low-frequency region of the EIS spectra (0.1 to 1.0 Hz). Figure 5b and Figure 5c displays the relationship between the real impedance and the angular frequency of the measurements, and the equation used to calculate D_{Na}, respectively. These results demonstrate that the cPAN layer improves the Na-ion diffusion for the ensemble electrode to which it is applied.

Thus far, the cPAN-protective layer has been shown to increase the achievable capacity of the ensemble electrode, resulting from the charge storage properties of the cPAN, and has acted to reduce the R_{ct} of the electrode (due to the conductive properties of the polymer layer) while enhancing the ensemble electrode's D_{Na}. The cPAN layer has also been shown to affect the early cycle (de)sodiation chemistry of Sb and improve the rate capability of the electrode, both of which could result from differences in the surface chemistry imparted by the cPAN. Interestingly, the R_{SEI} values (Figure 4b) for the cPAN@Sb system was strikingly similar to the R_{SEI} of the Sb control, which implies that the surface chemistries of these systems are similar. To disprove the hypotheses that the differences in the early cycle (de)sodiation chemistry and enhanced rate capability of the cPAN system result from cPAN's effect on the surface chemistry of the Sb electrode, and to assess the R_{SEI} values seen in Figure 4b, characterization of the surface chemistry was conducted via X-ray photoelectron spectroscopy (XPS).

3.3. Characterization of Surface Chemistry. The surface chemistry of the cPAN@Sb and Sb systems after the first discharge and 10th cycle is not significantly different (particularly in the carbon environments) to account for the differences in the electrochemical and resistive phenomena between the cPAN@Sb and Sb systems. XPS was conducted on the cPAN@Sb and Sb systems for pristine electrodes, electrodes after the first discharge cycle, and electrodes after the 10th cycle to evaluate the effect of cPAN on the surface chemistry of the Sb active material. Figure 6 displays the high-resolution XPS spectra of the C 1s environments for the cPAN@Sb and Sb systems for pristine, after first discharge, and after the 10th cycle electrode conditions.

The C 1s spectrum for the pristine cPAN (Figure 6a) system shows peaks at 285, 286.58, 287.77, and 289.01 eV, which relate to C−C, C−N, C═N, and CO_2 environments, respectively. The C−C environments for the pristine system relate to the C−C bonds in the polymer backbone of the cPAN coating, with the C═N species resulting from the C═N bonds of the pyridine structure in cPAN.[12,28] The presence of C−N environments in the pristine cPAN sample could be indicative of a graphitic species in addition to pyridine structures, although these moieties are present at low levels.[46] The presence of both the C═N and C−N environments in the C 1s spectra is corroborated by the presence of corresponding C═N and C−N environments in the N 1s spectra (Figure S14). Exposure of the pristine cPAN@Sb sample to the air during sample transfer to the XPS instrument likely accounts for presence of environments related to CO_2 structures, which has been seen for pristine cPAN samples annealed under an argon atmosphere in the past.[33] Concerning the C 1s spectrum for the pristine Sb (Figure 6d) system, the main environments present relate to C−C and C−O structures, at roughly 285 and 286 eV, respectively. These environments result from adventitious carbon, which is common for all XPS experiments (even on systems that do not contain carbon), and are in good agreement with previous XPS characterization of pristine Sb films.[35,47] Concerning the overlapping O 1s and Sb 3d environments for the pristine cPAN system, the presence of Sb_2O_3, indicated by the peak at 540 eV in Figure S15a, is in good agreement with the postannealing PXRD analysis from Figure 1b. These overlapping O 1s and Sb 3d environments for the pristine cPAN system also contain a peak at roughly 532 eV, which relates to presence of C−O constituents on the surface, consistent with what is seen in Figure 6a. Regarding the pristine Sb system, the overlapping O 1s and Sb 3d environments clearly indicate the presence of Sb_2O_3 via peaks at 540 eV (Sb_2O_3 3/2) and 531 eV (Sb_2O_3 5/2) (Figure S15d), which is in good agreement with the results summarized in Figure 1b.

The C 1s spectra for the cPAN system after the first discharge step (Figure 6b) show an increase in the presence of C−O bonding environments (CO_3 at 291 eV and CO_2 at 289.5 eV), which is expected due to the electrolyte reduction to form the initial SEI during the first discharge half cycle.[48] These environments are corroborated by a peak at 531 eV in the overlapping O 1s and Sb 3d environments, as seen in Figure S15b, related to the C−O environments. The presence of binding environments at 534 eV in Figure S15b relate to either a CO_2 or ClO_4 species, both of which are expected in the SEI after the first discharge half cycle.[48] Regarding the C−N environments, the C 1s spectrum demonstrates a decrease in the presence of the C−N and C═N environments. In the N 1s spectrum, the C−N and C═N environments are still present, which indicates that although the organic component of the SEI increases after the first discharge cycle, the SEI is not so thick that the nitrogen environments from the cPAN layer are undetectable. Future work will test this hypothesis via XPS sputtering experiments aimed at characterizing the thickness of the SEI layer in relation to the cPAN coating. Concerning the Sb system after the first-discharge cycle (Figure 6e), the C 1s spectrum displays a sharp increase of CO_3 compounds in the SEI, in addition to an increase in the presence of C−O signatures, which are corroborated via the XPS spectrum for the overlapping O 1s and Sb 3d environments (Figure S15e) in the form of C═O and C−O signatures. The overlapping O 1s and Sb 3d environments also show the presence of either CO_2 and/or ClO_4. These increases in the CO_3 and C−O environments, and the presence of CO_2 and/or ClO_4, are common for the initial SEI formation, which occurs during the first discharge cycle in these systems.[22,48] Upon comparison of the first discharge C 1s spectra for the cPAN and Sb, it is clear to see that the Sb system has a surface layer with a higher extent of C−O bond containing compounds. The compositional differences in the first discharge SEI (Figure 6b and Figure 6e) help to explain the first cycle discharge traces in Figure 3c and Figure 3d, which supports the hypothesis that the cPAN layer is affecting the composition of the initial SEI. These compositional differences could arise for several reasons, including increased surface area of the cPAN compared to the Sb (Figure S7), chemical interactions between the cPAN and the electrolyte, or the higher R_{ct} of the pristine cPAN system compared to Sb. These hypotheses will be the focus of future investigations into the role of cPAN in the early cycle surface chemistry of Sb electrodes.

The C 1s spectra for the cPAN and Sb after the 10th cycle are dominated by the same species, namely, CO_3, CO_2, C−O, and C−C environments (Figure 6c,f). Concerning the cPAN system specifically, the C−N and C═N environments disappear with a commensurate increase in the peaks relating

https://doi.org/10.1021/acsami.4c13887
ACS Appl. Mater. Interfaces 2025, 17, 2117−2129

to the carbon−oxygen environments, which is easily rationalized by a growth in the SEI layer from the 1st cycle to the 10th cycle.[49] The presence of carbon−oxygen species in the C 1s spectra is supported by the spectra for the overlapping O 1s and Sb 3d environments (Figure S15c,f). As shown in Figure S15f, peaks at 537 and 528 eV relate to Sb3/2 and Sb5/2 environments, respectively. These environments likely arise in the spectrum from the breakdown of the SEI layer, which could occur from the washing procedure or localized fracturing of the SEI (particularly since there are no peaks related to Sb in Figure S15e). The similarities in the C 1s spectra between the cPAN and Sb systems (after the 10th cycle) help to support the R_{SEI} values from Figure 4b, where the SEI resistance values were similar for both the cPAN and Sb systems. These similarities also disprove the notion that the improved rate capability for the cPAN system (Figure 3b) results from differences in the surface chemistry. Thus, the cPAN layer does not significantly change or affect the composition of the as-formed organic components of the SEI at later cycle numbers.

Concerning the inorganic components of the SEI, NaF is apparent in both the cPAN and Sb systems after both the first discharge and the 10th cycle, as seen by the peaks at roughly 684.9 and 1072 eV in the fluorine and sodium spectra, respectively (Figures S16 and S17). NaF is well understood to improve the as-formed SEI due to the mechanical and conductive properties of this material and forms from the decomposition of the FEC electrolyte additive.[21,48] Given that NaF is present in the SEI of both systems, after the first discharge and after 10 cycles, we can confirm that the enhanced R_{ct} (Figure 4a) for the cPAN system relates to the conductive properties of the coating and not from differences in the inorganic component of the as-formed SEIs.

4. CONCLUSIONS

In this work, we have characterized the multifunctionality of a cPAN coating on Sb-based anode materials in NIBs. The inclusion of a cPAN layer increases the achievable capacity of the electrode system to which it is applied and increases the capacity retention as a function of rate. These results arise from the ability of cPAN to actively store Na ions and its ability to increase the hardness of the material to which it is applied, respectively. The cPAN coating also helps to facilitate the transfer of Na ions from the electrolyte to the Sb active material because of the conductive nature of the polymer, which becomes more conductive as the battery is cycled. This, also, leads to an increase in the D_{Na} of the cPAN-coated electrode compared to a bare Sb-based system.

The cPAN coating, interestingly, provided for a worse cycle life compared to the Sb control system despite the deep literature understanding of cPAN as a protective coating. This result likely stems from the layered coating-active material configuration used in this investigation for the purpose of studying the fundamental effect of cPAN on Sb electrodes in NIBs. The worse cycle life for the layered cPAN@Sb electrode, in conjunction with the literature on cPAN in batteries, implies that cPAN needs to be applied to nanoscale active materials or used to form a composite electrode to impart improvement to the cycle life of the active materials.

The cPAN layer most affects the early cycle (de)sodiation chemistry of the Sb electrode to which it is applied. This result is somewhat in line with the initial hypothesis that the cPAN layer would affect the (de)sodation chemistry of the Sb electrode. Yet, the (de)sodiation chemistry of the cPAN@Sb and Sb systems is strikingly similar at higher cycle numbers. This trend is mirrored in the XPS analysis of the SEI of the cPAN and Sb systems, where the largest differences in the as-formed SEI are present after the first discharge half cycle. By the time the electrodes reach the 10th cycle, the organic and inorganic components of the SEIs for both the cPAN and Sb systems are similar, implying that the properties of cPAN, which impart the early cycle differences in the (de)sodiation and surface chemistry of Sb, are no longer present at higher cycle numbers. Future investigations should focus on quantifying the constituents present in the early cycle SEI of cPAN-coated electrodes to assess exactly how the resistive properties of cPAN effect the as-formed SEI, providing insight into the relationship between SEI formation and the conductive properties of the electrode in NIBs. This information will provide fundamental insight that will aid in design principles for CPBs as protective coatings for conversion electrodes in NIBs.

■ ASSOCIATED CONTENT

Supporting Information

The Supporting Information is available free of charge at https://pubs.acs.org/doi/10.1021/acsami.4c13887.

Schematic representation for anode stability; elemental mapping of preannealed Sb electrode; X-ray diffraction data and Rietveld refinement data; cross-sectional imaging of cPAN; cyclic voltammograms for ECSA; images and box plot of Vickers hardness testing; table and equivalent circuit model for impedance analysis; optical images, FITR analysis, cycle life plot, and dQ/dV plot for cPAN slurry electrodes; polarization curves and dQ/dV plots from CCCV+EIS experiments; EIS Nyquist plots from CCCV+EIS experiments; tables with fitted values from CCCV+EIS analysis; and XPS environments (PDF)

■ AUTHOR INFORMATION

Corresponding Author

Amy L. Prieto − *Department of Chemistry, Colorado State University, Fort Collins, Colorado 80523, United States; School of Materials Science and Engineering, Colorado State University, Fort Collins, Colorado 80523, Unites States;* orcid.org/0000-0001-9235-185X; Email: amy.prieto@colostate.edu

Authors

Daniel S. Windsor − *Department of Chemistry, Colorado State University, Fort Collins, Colorado 80523, United States*

Monika J. Perez − *Department of Chemistry, Colorado State University, Fort Collins, Colorado 80523, United States*

Erin R. Snyder − *Department of Chemistry, Colorado State University, Fort Collins, Colorado 80523, United States*

Nathan A. Neisius − *Department of Chemistry, Colorado State University, Fort Collins, Colorado 80523, United States;* orcid.org/0000-0002-0454-6970

Rhys A. Otten − *School of Materials Science and Engineering, Colorado State University, Fort Collins, Colorado 80523, Unites States*

Sarah C. Hall − *Department of Chemistry, Colorado State University, Fort Collins, Colorado 80523, United States*

Clara A. Tibbetts − *Department of Chemistry, Colorado State University, Fort Collins, Colorado 80523, United States*

https://doi.org/10.1021/acsami.4c13887
ACS Appl. Mater. Interfaces 2025, 17, 2117−2129

Amber T. Krummel − *Department of Chemistry, Colorado State University, Fort Collins, Colorado 80523, United States;* orcid.org/0000-0003-3973-1575

Complete contact information is available at: https://pubs.acs.org/10.1021/acsami.4c13887

Author Contributions

D.S.W. developed initial hypotheses, designed experiments, analyzed data, and led the writing of the manuscript. M.J.P. performed XPS data analysis and assisted with writing the manuscript. E.R.S. performed XPS analysis and assisted with writing the manuscript. N.A.N. performed PXRD and SEM analyses and contributed with writing the manuscript. R.A.O. collected and analyzed the data for the Vickers hardness test and assisted in writing the manuscript. S.C.H. and C.A.T. collected the FTIR data, and S.C.H. assisted in writing the manuscript. A.T.K. provided insight on the analysis of the FTIR data. A.L.P. assisted with conceptualization of the project, data interpretation, and editing of the manuscript.

Funding

This work was funded by the National Science Foundation (Award #2211067).

Notes

The authors declare no competing financial interest.

■ ACKNOWLEDGMENTS

We would like to acknowledge the National Science Foundation for financial support for this project. We also acknowledge the CSU Analytical Resources Core facilities for use of their space and facilities (SCR_021758). Special thanks are given to Dr. Rebecca Millar of the Analytical Resource Core for help with SEM and XPS.

■ REFERENCES

(1) Winter, M.; Brodd, R. J. What Are Batteries, Fuel Cells, and Supercapacitors? *Chem. Rev.* **2004**, *104* (10), 4245−4269.

(2) Goodenough, J. B.; Kim, Y. Challenges for Rechargeable Li Batteries. *Chem. Mater.* **2010**, *22* (3), 587−603.

(3) Rapier, R. *Funding For Battery Technology Companies Exploded in 2020*; Forbes. https://www.forbes.com/sites/rrapier/2021/02/06/funding-for-battery-technology-companies-exploded-in-2020/?sh=30fa8e4e33ab (accessed 2022−05−12).

(4) Rathi, A.; Murray, P.; Dottle, R. *The Hidden Science Making Batteries Better, Cheaper and Everywhere*; Bloomberg Green. https://www.bloomberg.com/graphics/2021-inside-lithium-ion-batteries/ (accessed 2022−12−02).

(5) Harper, G.; Sommerville, R.; Kendrick, E.; Driscoll, L.; Slater, P.; Stolkin, R.; Walton, A.; Christensen, P.; Heidrich, O.; Lambert, S.; Abbott, A.; Ryder, K.; Gaines, L.; Anderson, P. Recycling Lithium-Ion Batteries from Electric Vehicles. *Nature* **2019**, *575* (7781), 75−86.

(6) Peng, L.; Zhu, Y.; Chen, D.; Ruoff, R. S.; Yu, G. Two-Dimensional Materials for Beyond-Lithium-Ion Batteries. *Adv. Energy Mater.* **2016**, *6* (11), No. 1600025.

(7) Sarkar, S.; Peter, S. C. An Overview on Sb-Based Intermetallics and Alloys for Sodium-Ion Batteries: Trends, Challenges and Future Prospects from Material Synthesis to Battery Performance. *J. Mater. Chem. A* **2021**, *9*, 5164−5196.

(8) Hirsh, H. S.; Li, Y.; Tan, D. H. S.; Zhang, M.; Zhao, E.; Meng, Y. S. Sodium-Ion Batteries Paving the Way for Grid Energy Storage. *Adv. Energy Mater.* **2020**, *10* (32), No. 2001274.

(9) US Department of the Interior *Mineral Commodity Summaries 2023*; US Geological Survey, 2023; pp 1−210. https://pubs.usgs.gov/publication/mcs2023.

(10) Dunlap, N. A.; Kim, J.; Guthery, H.; Jiang, C.-S.; Morrissey, I.; Stoldt, C. R.; Oh, K. H.; Al-Jassim, M.; Lee, S.-H. Towards the Commercialization of the All-Solid-State Li-Ion Battery: Local Bonding Structure and the Reversibility of Sheet-Style Si-PAN Anodes. *J. Electrochem. Soc.* **2020**, *167* (6), No. 060522.

(11) Piper, D. M.; Evans, T.; Leung, K.; Watkins, T.; Olson, J.; Kim, S. C.; Han, S. S.; Bhat, V.; Oh, K. H.; Buttry, D. A.; Lee, S. H. Stable Silicon-Ionic Liquid Interface for next-Generation Lithium-Ion Batteries. *Nat. Commun.* **2015**, *6* (6230), 1−10.

(12) Piper, D. M.; Yersak, T. A.; Son, S. B.; Kim, S. C.; Kang, C. S.; Oh, K. H.; Ban, C.; Dillon, A. C.; Lee, S. H. Conformal Coatings of Cyclized-PAN for Mechanically Resilient Si Nano-Composite Anodes. *Adv. Energy Mater.* **2013**, *3* (6), 697−702.

(13) Mosby, J. M.; Prieto, A. L. Direct Electrodeposition of Cu2Sb for Lithium-Ion Battery Anodes. *J. Am. Chem. Soc.* **2008**, *130* (32), 10656−10661.

(14) Schulze, M. C.; Belson, R. M.; Kraynak, L. A.; Prieto, A. L. Electrodeposition of Sb/CNT Composite Films as Anodes for Li- and Na-Ion Batteries. *Energy Storage Mater.* **2020**, *25*, 572−584.

(15) Zheng, X. M.; You, J. H.; Fan, J. J.; Tu, G. P.; Rong, W. Q.; Li, W. J.; Wang, Y. X.; Tao, S.; Zhang, P. Y.; Zhang, S. Y.; Shen, S. Y.; Li, J. T.; Huang, L.; Sun, S. G. Electrodeposited Binder-Free Sb/NiSb Anode of Sodium-Ion Batteries with Excellent Cycle Stability and Rate Capability and New Insights into Its Reaction Mechanism by Operando XRD Analysis. *Nano Energy* **2020**, *77*, No. 105123.

(16) Nieto, K.; Gimble, N. J.; Rudolph, L. J.; Kale, A. R.; Prieto, A. L. Electrodeposition vs Slurry Casting: How Fabrication Affects Electrochemical Reactions of Sb Electrodes in Sodium-Ion Batteries. *J. Electrochem. Soc.* **2022**, *169* (5), No. 050537.

(17) He, J.; Wei, Y.; Zhai, T.; Li, H. Antimony-Based Materials as Promising Anodes for Rechargeable Lithium-Ion and Sodium-Ion Batteries. *Mater. Chem. Front.* **2018**, *2* (3), 437−455.

(18) Caputo, R. An Insight into Sodiation of Antimony from First-Principles Crystal Structure Prediction. *J. Electron. Mater.* **2016**, *45* (2), 999−1010.

(19) Ma, W.; Wang, J.; Gao, H.; Niu, J.; Luo, F.; Peng, Z.; Zhang, Z. A Mesoporous Antimony-Based Nanocomposite for Advanced Sodium Ion Batteries. *Energy Storage Mater.* **2018**, *13*, 247−256.

(20) Dashairya, L.; Das, D.; Saha, P. Binder-Free Electrophoretic Deposition of Sb/rGO on Cu Foil for Superior Electrochemical Performance in Li-Ion and Na-Ion Batteries. *Electrochim. Acta* **2020**, *358*, No. 136948.

(21) Jung, R.; Metzger, M.; Haering, D.; Solchenbach, S.; Marino, C.; Tsiouvaras, N.; Stinner, C.; Gasteiger, H. A. Consumption of Fluoroethylene Carbonate (FEC) on Si-C Composite Electrodes for Li-Ion Batteries. *J. Electrochem. Soc.* **2016**, *163* (8), A1705−A1716.

(22) Bodenes, L.; Darwiche, A.; Monconduit, L.; Martinez, H. The Solid Electrolyte Interphase a Key Parameter of the High Performance of Sb in Sodium-Ion Batteries: Comparative X-Ray Photoelectron Spectroscopy Study of Sb/Na-Ion and Sb/Li-Ion Batteries. *J. Power Sources* **2015**, *273*, 14−24.

(23) Li, J.; Cai, Y.; Wu, H.; Yu, Z.; Yan, X.; Zhang, Q.; Gao, T. Z.; Liu, K.; Jia, X.; Bao, Z. Polymers in Lithium-Ion and Lithium Metal Batteries. *Adv. Energy Mater.* **2021**, *11* (15), 2−47.

(24) Dunlap, N. A.; Kim, J.; Oh, K. H.; Lee, S.-H. Slurry-Coated Sheet-Style Sn-PAN Anodes for All-Solid-State Li-Ion Batteries. *J. Electrochem. Soc.* **2019**, *166* (6), A915−A922.

(25) Datta, M. K.; Kumta, P. N. Silicon and Carbon Based Composite Anodes for Lithium Ion Batteries. *J. Power Sources* **2006**, *158* (1), 557−563.

(26) Leroy, S.; Boiziau, C.; Perreau, J.; Reynaud, C.; Zalczer, G.; Lécayon, G.; Le Gressus, C. Molecular Structure of Electropolymerized Polyacrylonitrile Film and Its Pyrolyzed Derivatives. *J. Mol. Struct.* **1985**, *128*, 269−281.

(27) Xue, T. J.; Mckinney, M. A.; Wilkie, C. A. The Thermal Degradation of Polyacrylonitrile. *Polym. Degredation Stab.* **1997**, *58*, 193−202.

(28) Zhang, W.; Sun, M.; Yin, J.; Abou-Hamad, E.; Schwingenschlögl, U.; Costa, P. M. F. J.; Alshareef, H. N. A Cyclized Polyacrylonitrile Anode for Alkali Metal Ion Batteries. *Angew. Chem. - Int. Ed.* **2021**, *60* (3), 1355−1363.

(29) Liu, Q.; Xiao, Z.; Cui, X.; Deng, S.; He, Q.; Zhang, Q.; Lin, Z.; Yang, Y. Conjugated Cyclized-Polyacrylonitrile Encapsulated Carbon Nanotubes as Core-Sheath Heterostructured Anodes with Favorable Lithium Storage. *J. Mater. Chem. A* **2021**, *9* (11), 6962−6970.
(30) Gimble, N.; Nieto, K.; Prieto, A. Electrodeposition as a Powerful Tool for the Fabrication and Characterization of Next-Generation Anodes for Sodium Ion Rechargeable Batteries. *Electrochem. Soc. Interface* **2021**, *30* (50), 59−63.
(31) Pitschke, W.; Hermann, H.; Mattern, N. The Influence of Surface Roughness on Diffracted X-Ray Intensities in Bragg−Brentano Geometry and Its Effect on the Structure Determination by Means of Rietveld Analysis. *Powder Diffr.* **1993**, *8* (2), 74−83.
(32) Schneider, J. D.; Agocs, D. B.; Prieto, A. L. Design of a Sample Transfer Holder to Enable Air-Free X-Ray Photoelectron Spectroscopy. *Chem. Mater.* **2020**, *32* (19), 8091−8096.
(33) Schulze, M. C.; Prieto, A. L. Mixed-Conducting Properties of Annealed Polyacrylonitrile Activated by n-Doping of Conjugated Domains. *Chem. Sci.* **2021**, *13* (1), 225−235.
(34) Arbab, S.; Mirbaha, H.; Zeinolebadi, A.; Nourpanah, P. Indicators for Evaluation of Progress in Thermal Stabilization Reactions of Polyacrylonitrile Fibers. *J. Appl. Polym. Sci.* **2014**, *131* (11), 8.
(35) Nieto, K.; Windsor, D. S.; Kale, A. R.; Gallawa, J. R.; Medina, D. A.; Prieto, A. L. Structural Control of Electrodeposited Sb Anodes through Solution Additives and Their Influence on Electrochemical Performance in Na-Ion Batteries. *J. Phys. Chem. C* **2023**, *127* (26), 12415−12427.
(36) Schulze, M. C.; Schulze, R. K.; Prieto, A. L. Electrodeposited Thin-Film Cu:XSb Anodes for Li-Ion Batteries: Enhancement of Cycle Life via Tuning of Film Composition and Engineering of the Film-Substrate Interface. *J. Mater. Chem. A* **2018**, *6* (26), 12708−12717.
(37) Asryan, N. A.; Alikhanyan, A. S.; Nipan, G. D. P−T−x Phase Diagram of the Sb−O System. *Inorg. Mater.* **2004**, *40* (6), 626−631.
(38) Gierlotka, W.; Jendrzejczyk-Handzlik, D. Thermodynamic Description of the Cu−Sb Binary System. *J. Alloys Compd.* **2009**, *484* (1−2), 172−176.
(39) Bryngelsson, H.; Eskhult, J.; Nyholm, L.; Edström, K. Thin Films of Cu2Sb and Cu9Sb2 as Anode Materials in Li-Ion Batteries. *Electrochim. Acta* **2008**, *53* (24), 7226−7234.
(40) Firdu, F. T.; Taskinen, P. *Thermodynamics and Phase Equilibria in the (Ni, Cu, Zn)-(As, Sb, Bi)-S Systems at Elevated Temperatures (300 − 900 °C)*; Aalto University School of Science and TechnologyDepartment of Materials Science and Engineering: **2010**, 8-48.
(41) Moon, J.; Jung, J. Y.; Hoang, T. D.; Rhee, D. Y.; Lee, H. B.; Park, M.-S.; Yu, J.-S. The Correlation between Particle Hardness and Cycle Performance of Layered Cathode Materials for Lithium-Ion Batteries. *J. Power Sources* **2021**, *486*, No. 229359.
(42) Lalau, C. C.; Low, C. T. J. Electrophoretic Deposition for Lithium-Ion Battery Electrode Manufacture. *Batter. Supercaps* **2019**, *2* (6), 551−559.
(43) Gimble, N. J.; Prieto, A. L. Spontaneous Solid Electrolyte Interface Formation in Uncycled Sodium Half-Cell Batteries: Using X-Ray Photoelectron Spectroscopy to Explore the Pre-Passivation of Sodium Metal by Fluoroethylene Carbonate before Potentials Are Applied. *Sustain. Energy Fuels* **2022**, *6* (20), 4736−4740.
(44) Wang, L.; Zhao, J.; He, X.; Gao, J.; Li, J.; Wan, C.; Jiang, C. Electrochemical Impedance Spectroscopy (EIS) Study of LiNi1/3Co1/3Mn1/3O2 for Li-Ion Batteries. *Int. J. Electrochem. Sci.* **2012**, *7* (1), 345−353.
(45) Meddings, N.; Heinrich, M.; Overney, F.; Lee, J.-S.; Ruiz, V.; Napolitano, E.; Seitz, S.; Hinds, G.; Raccichini, R.; Gaberšček, M.; Park, J. Application of Electrochemical Impedance Spectroscopy to Commercial Li-Ion Cells: A Review. *J. Power Sources* **2020**, *480*, No. 228742.
(46) Son, S.-B.; Gao, T.; Harvey, S. P.; Steirer, K. X.; Stokes, A.; Norman, A.; Wang, C.; Cresce, A.; Xu, K.; Ban, C. An Artificial Interphase Enables Reversible Magnesium Chemistry in Carbonate Electrolytes. *Nat. Chem.* **2018**, *10* (5), 532−539.
(47) Gengenbach, T. R.; Major, G. H.; Linford, M. R.; Easton, C. D. Practical Guides for X-Ray Photoelectron Spectroscopy (XPS): Interpreting the Carbon 1s Spectrum. *J. Vac. Sci. Technol. Vac. Surf. Films* **2021**, *39* (1), No. 013204.
(48) Gimble, N. J.; Kraynak, L. A.; Schneider, J. D.; Schulze, M. C.; Prieto, A. L. X-Ray Photoelectron Spectroscopy as a Probe for Understanding the Potential-Dependent Impact of Fluoroethylene Carbonate on the Solid Electrolyte Interface Formation in Na/Cu2Sb Batteries. *J. Power Sources* **2021**, *489*, No. 229171.
(49) Darwiche, A.; Bodenes, L.; Madec, L.; Monconduit, L.; Martinez, H. Impact of the Salts and Solvents on the SEI Formation in Sb/Na Batteries: An XPS Analysis. *Electrochim. Acta* **2016**, *207*, 284−292.

https://doi.org/10.1021/acsami.4c13887
ACS Appl. Mater. Interfaces 2025, 17, 2117−2129